Environmental Nanotechnology, Monitoring & Management 16 (2021) 100598

Contents lists available at ScienceDirect

Environmental Nanotechnology, Monitoring & Management

journal homepage: www.elsevier.com/locate/enmm

Facile synthesis of hierarchical porous ZIF-8@TiO2 for simultaneous adsorption and photocatalytic decomposition of crystal violet

Stefanny Angela [a], Valentino Bervia Lunardi [a], Karissa Kusuma [a], Felycia Edi Soetaredjo [a,b,*], Jindrayani Nyoo Putro [a], Shella Permatasari Santoso [a,b], Artik Elisa Angkawijaya [b], Jenni Lie [a], Chintya Gunarto [a], Alfin Kurniawan [a], Suryadi Ismadji [a,b,*]

[a] *Department of Chemical Engineering, Widya Mandala Surabaya Catholic University, Kalijudan 37, Surabaya 60114, Indonesia*
[b] *Department of Chemical Engineering, National Taiwan University of Science and Technology, No. 43, Sec. 4, Keelung Rd., Da'an District, Taipei City, Taiwan*

ARTICLE INFO

Keywords:
Adsorption
Photocatalytic
Degradation

ABSTRACT

In this study, a facile one-pot method was developed to create hierarchical porous M−ZIF−8 by utilizing NaOH as a defecting agent. The as-synthesized material comprising macroporous and mesoporous and exhibits hierarchical porosity. TiO_2 (anatase) with different mass ratios (5%, 15%, and 25%) were immobilized into M−ZIF−8 to combine the synergism of adsorption and photocatalytic oxidation. Five percent of TiO_2 immobilized in M−ZIF−8 gave the best adsorption and photocatalytic degradation. The adsorption kinetics and isotherms of CV on M−ZIF−8 were also evaluated to validate the adsorption capability of M−ZIF−8. After four consecutive experiments, the adsorption and photocatalytic performance of M−ZIF−8@TiO_2 to degrade CV slightly decreased.

1. Introduction

Advanced Oxidation Processes (AOPs) are regarded as one of the most-efficacy techniques in hazardous substances elimination from wastewater compared to other commonly employed wastewater treatment processes (Miklos et al., 2018). AOPs offer several advantages, including facile operation at or near ambient pressure and temperature and transform roughly all the contained organic contaminants in effluents into less hazardous substances (Kanakaraju et al., 2018). Various processes such as Fenton (Lu et al., 2021) and photo-Fenton catalytic reaction (Vorontsov, 2019), processes using H_2O_2 or UV-Irradiation (Yang et al., 2017), as few instances of AOPs, counts as the efficient techniques through hydroxyl radical's production which oxidizes non-selectively extensive range of organic contaminant in wastewater.

The utilization of photocatalytic degradation under UV/Visible irradiation appears as a green technique in wastewater treatment, particularly in dye degradation. Variety photocatalyst substances such as TiO2 (Chen et al., 2020), ZrO2 (Chen et al., 2020), and ZnO (Ong et al., 2018) have been utilized for pollutants elimination. TiO2 is the most promising photocatalysts among diverse photocatalysts due to superior photostability, minimum production cost, excellent intrinsic catalytic activity under UV-Irradiation, and non-toxic and harmful towards both environment and humans (Abdi et al., 2019). Nevertheless, the photocatalytic activity of pure TiO_2 experienced two significant shortcomings: firstly, pure TiO_2 can limit the influence of catalytic activity on account of the nanospheres aggregation; Secondly, rapid recombination of photo-induced electrons and holes weaken the photo-induced redox reaction. Thereby, how to tackle the TiO_2 aggregation and dwindled the recombination rate of photo-induced electrons and holes emerged as our research focus. Incorporating the semiconductor towards other porous materials may overcome the major drawbacks and enhance photocatalytic performance.

One of the engineered materials, namely metal-organic framework (MOF), has received significant attention owing to the high surface area, high porosity, and structural versatility. MOFs are inorganic-organic hybrid materials with the porous framework constructed by self-assembly between the metal cluster or polynuclear secondary building units (SBUs) and organic ligands (Joseph et al., 2019). Until now, over five thousand diverse MOFs structure have been constructed on record at Cambridge Crystallographic Data Centre (Furukawa et al., 2013), showing outstanding performance towards several fields such as adsorption, catalyst, chemical separation, gas storage, and sensors. However, regardless of the structural flexibility and rich chemistry, mostly the recently published MOFs having microporous structure (pore

---

* Corresponding authors at: Department of Chemical Engineering, Widya Mandala Surabaya Catholic University, Kalijudan 37, Surabaya 60114, Indonesia.
E-mail addresses: felyciae@yahoo.com (F. Edi Soetaredjo), suryadiismadji@yahoo.com (S. Ismadji).

https://doi.org/10.1016/j.enmm.2021.100598
Received 2 July 2021; Received in revised form 21 September 2021; Accepted 12 October 2021

sizes <1 nm) consequently restraint the diffusion of the bulky molecules and limits the accessibility of open channel or MOFs active sites (Guan et al., 2018). Hence, the methodology of enlarging the pore size for mass transfer improvement and refine the accessibility of active sites are highly required.

Various processes have been developed to synthesize mesoporous MOFs, such as ligand extension, ligand mixing, post-treatment, and templating techniques (Guan et al., 2018). Regrettably, most of the mentioned methodology requires complex techniques, long-time processes, and high-cost reagents, hindering practical and production feasibility. For ligand mixing and ligand extension methods, it required diverse ligands to elongate the distance between metal centers which induce complexity and unpredictability of as-synthesized MOFs: the complex fabrication, cautious activation, and structural metastability. Thereby, it is required a simplified method to introduce mesoporous structure in micropores of MOFs.

Different approaches have been advanced to simplify introducing the mesopores into imidazolates-based MOFs with microporous structure, Zeolitic Imidazolate Framework (ZIF-8). In general, ZIF-8 is a hybrid engineered material with a porous structure analogous to zeolites constructed through 4-connected nets of tetrahedral units where Zn^{2+} as metal cluster coordinated to N atoms in diatopic imidazolate anions. ZIF-8 presents a sod topology consisted of 1.16 nm cages connected through 0.34 nm six-membered windows (Fig. 1(a and b)). Zhang's groups (Zhang et al., 2015) developed sequent synthesis through nanoparticle encapsulation followed by the etching method to develop the mesopores structure of ZIF-8. Jing et al. (Jing et al., 2018) utilized polystyrene as a template to construct hierarchical ZIF-8 with micro-, meso-, and macropores structure. Li's and Jhung's groups (Wu et al., 2014; Jung et al., 2015) fabricate hierarchical ZIF-8 with micro-and mesopores structure by utilizing cetyltrimethylammonium bromide (CTAB) amino-acid L-histidine as co-template. Chou et al. (Chou et al., 2015) put forward a double solvent mediate overgrowth mechanism for the hollow and mesoporous structure of ZIF-8 construction. A work by Chen et al. (Chen et al., 2019) through facile one-pot synthesis with the utilization of poly(diallyl dimethylammonium chloride) (PDDA) as the structure-directing agent to construct hierarchical meso-,macroporous of ZIF-8 porosity. Unfortunately, all of this method required expensive reagents and relatively complicated procedures to utilize.

In this work, we successfully develop facile synthesis through a one-step approach method of construct hierarchical ZIF-8 with meso-,macroporous structure with the addition of sodium hydroxide (NaOH). This approach has been in line with tailoring MOF materials for photocatalytic activity through hosting the TiO_2 materials in a porous framework. Incorporating TiO_2 into zeolites or coating TiO_2 with other substances and similar techniques has been widely adopted recently (Wang et al., 2014; Xu et al., 2018). The utilization of covered TiO_2 NPs frequently diminishes the catalytic activity owing to limited access towards dissolved organic dyes (Chandra et al., 2016). Meanwhile, Immobilization and encapsulation techniques of TiO_2 NPs into inorganic substances provide more effective catalytic activity despite having stability issues with zeolites as typical inorganic hosts (Liu et al., 2014). Since ZIF-8 exhibits thermal and chemical stability with mesoporous structure, this material was chosen as the host for TiO_2 encapsulation. Photocatalytic activity of ZIF-8 and I ts nanomaterials composite has been widely explored utilizing UV-Irradiation, for instance: ZnO@ZIF-8 (Akbari Beni et al., 2020; Yang et al., 2018), Ag/AgCl@ZIF-8 (Fan et al., 2018), Pt@ZIF-8, and $CulnS_2$@ZIF-8 (Liu et al., 2019). It was observed, the M−ZIF−8@TiO_2 composite provides synergism catalytic activity through simultaneous adsorption and photocatalytic degradation. Due to its mesoporous structure of M−ZIF−8, M−ZIF−8 presents excellent adsorption ability by improving the active site accessibility and molecular diffusion to extend the contact time between catalyst and crystal violet (CV) and elevate the ability of CV degradation. Moreover, TiO_2 was homogenously incorporated into the M−ZIF−8 pore and constructed N-Ti-O bond under facile synthesis treatment, preventing fast recombination of the electron-hole pairs and aggregation of TiO_2 nanomaterials photocatalytic system. Because of the unique porosity of the M−ZIF−8@TiO_2 composites and the chemical bonded M−ZIF−8@TiO_2, this composite improved the photocatalytic activity of crystal violet degradation while maintaining its thermal stability and crystallinity after post-modification.

2. Materials and method

2.1. Materials

The chemicals involved in this research including zinc sulphate heptahydrate ($ZnSO_4 \cdot 7H_2O$) (CAS:7446-20-0, 99.295%purity trace metal basis), 2-Methylimidazole (CAS: 693-98-1; 99%), sodium hydroxide (NaOH) (Analytical Reagent (AR) Grade; CAS: 1310-73-2; $\geq$ 98.5% purity) and Titanium (IV) oxide (TiO_2) (CAS: 1317-70-10) anatase grade, 99.8% trace metal basis), crystal violet ($C_{25}H_{30}N_5Cl$) (CAS:548-62-9; ACS Reagent $\geq$ 90.0% anhydrous basis, isopropyl

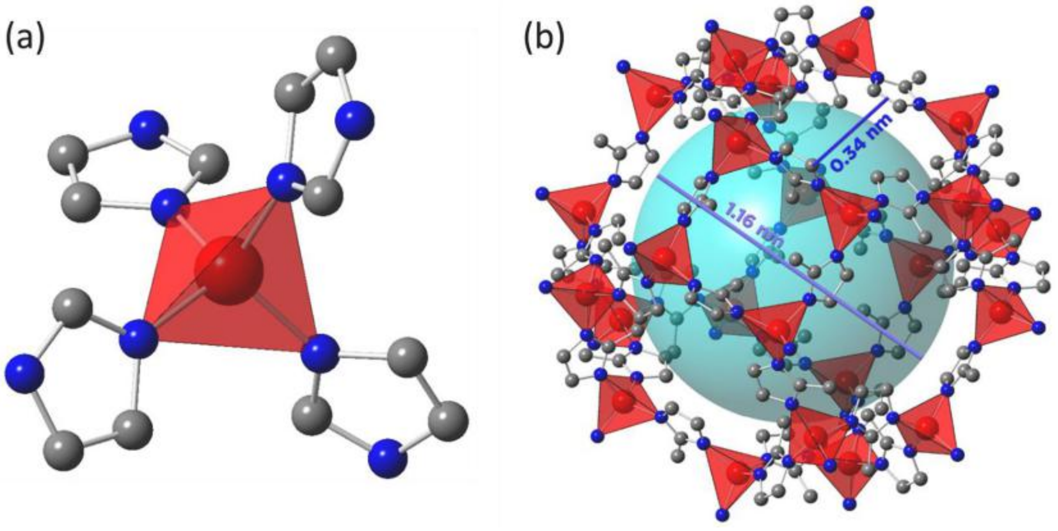

Fig. 1. Chemical structure of ZIF-8; (a) tetrahedron building units of M−ZIF−8 ($Zn(Hmim)_4$ Tetrahedron); (b) M−ZIF−8 architecture manifests cages with diameter 1.16 nm and six-membered windows with 0.34 nm. Molecular formula: Zn – Red, C – Gray, N – Blue. Notes that H atom does not appear in the structure figure to simplify the display of ZIF-8 Structures. (For interpretation of the references to color in this figure legend, the reader is referred to the web version of this article.)

alcohol (IPA) (CAS:67-63-0; ACS Reagent ≥ 99.5%), P-benzoquinone ($C_6H_4O_2$) (CAS:106–51-4; Reagent Grade ≥ 99.5%), carbon tetrachloride (CCl_4) (CAS: 56-23-5; Reagent Grade ≥ 99.9%) and ammonium oxalate monohydrate ($(NH_4)_2C_2O_4{\cdot}H_2O$) (CAS:106-51-4; ACS Reagent ≥ 99%). All chemicals were acquired from Sigma Aldrich, Singapore, and were subsequently utilized without any further purification.

2.2. *Fabrication of Macro-/Mesoporous ZIF-8 (M−ZIF−8) and M−ZIF−8@TiO₂ composite*

The M−ZIF−8 were assembled in an aqueous phase by simply mixing a solution of $ZnSO_4{\cdot}7H_2O$ and 2-Methyl Imidazolate with the addition of NaOH. Initially, a certain quantity of $ZnSO_4{\cdot}7H_2O$ was dissolved in 5 ml of DI water to create a 0.84 M solution. Subsequently, 16 ml solution (3.00 M) comprising of 2-methyl imidazole (Hmim) were mixed with 1.6 ml of solution A and the addition of 0.2 ml NaOH solution (0.1 M). Further, the deionized water was added to the mixture until the total volume of the solution was 50 ml, and the mixture was stirred at room temperature for one hour. The as-synthesized product was isolated by centrifugation, washed by DI water until the supernatant achieved neutral pH. The solid was evacuated and dried under vacuum at 60 °C for further composite preparation. A photocatalytic agent, TiO_2, was introduced into the system for preparing M−ZIF−8. A specific volume of TiO_2 solution was added in the as-mixed solution of M−ZIF−8 according to the weight ratio of TiO_2 (5%, 15%, and 25%), and the stirring was continued for one h. Prior to the synthesis, TiO_2 solutions were made by immersing 2 gr TiO_2 into 5 ml methanol assisted with ultrasonication for 1 h. The schematical procedure is depicted in Fig. 2(b). Pristine ZIF-8 and ZIF-8@TiO_2 (5%) were synthesized according to similar synthesis steps without NaOH addition.

2.3. *Characterization of M−ZIF−8 and M- ZIF-8@TiO₂*

M−ZIF−8 and M−ZIF8@TiO_2 composite were characterized using field emission scanning electron microscopy (FESEM), X-ray diffraction (XRD), nitrogen (N_2) adsorption − desorption isotherms, and Fourier transforms infrared (FTIR) spectroscopy. The powder X-ray diffraction patterns of M−ZIF−8 and M−ZIF8@TiO_2 were determined using Bruker D2 Phaser diffractometer equipped with a Cu Kα radiation source ($\lambda = 0.15406$ nm) in the 2θ range of 5 − 50° and a scan rate of 0.05°/s. SEM images were obtained by JEOL JSM-6500F field emission SEM at an accelerating voltage of 15.0 kV and a working distance of 9.7 mm. All solid samples were coated with thin layer platinum before the surface topography analysis using SEM. N_2 sorption isotherms at 77 K were measured by Micromeritics ASAP 2020 analyzer. Before the measurements, the samples were degassed at 200 °C for 12 h under a vacuum environment. FTIR spectra were recorded at a range wavenumber of 4000–500 cm^{-1} using Shimadzu 8400S spectrometer through the KBr pellet technique. X-ray photoelectron spectroscopy (XPS) was carried on VG Thermo ESCALAB Mark II to evaluate the elemental states of M−ZIF−8@TiO_2. The UV diffuse reflectance spectra (DRS) were measured on a UV–vis spectrophotometer (Hitachi U-4100) across a 200–800 nm wavelength range, with $BaSO_4$ as the reflectance standard. A conventional three-electrode cell comprising a working electrode, a Pt counter electrode, and a standard Ag/AgCl electrode reference electrode was used to evaluate transient photocurrent density on a CHI660B

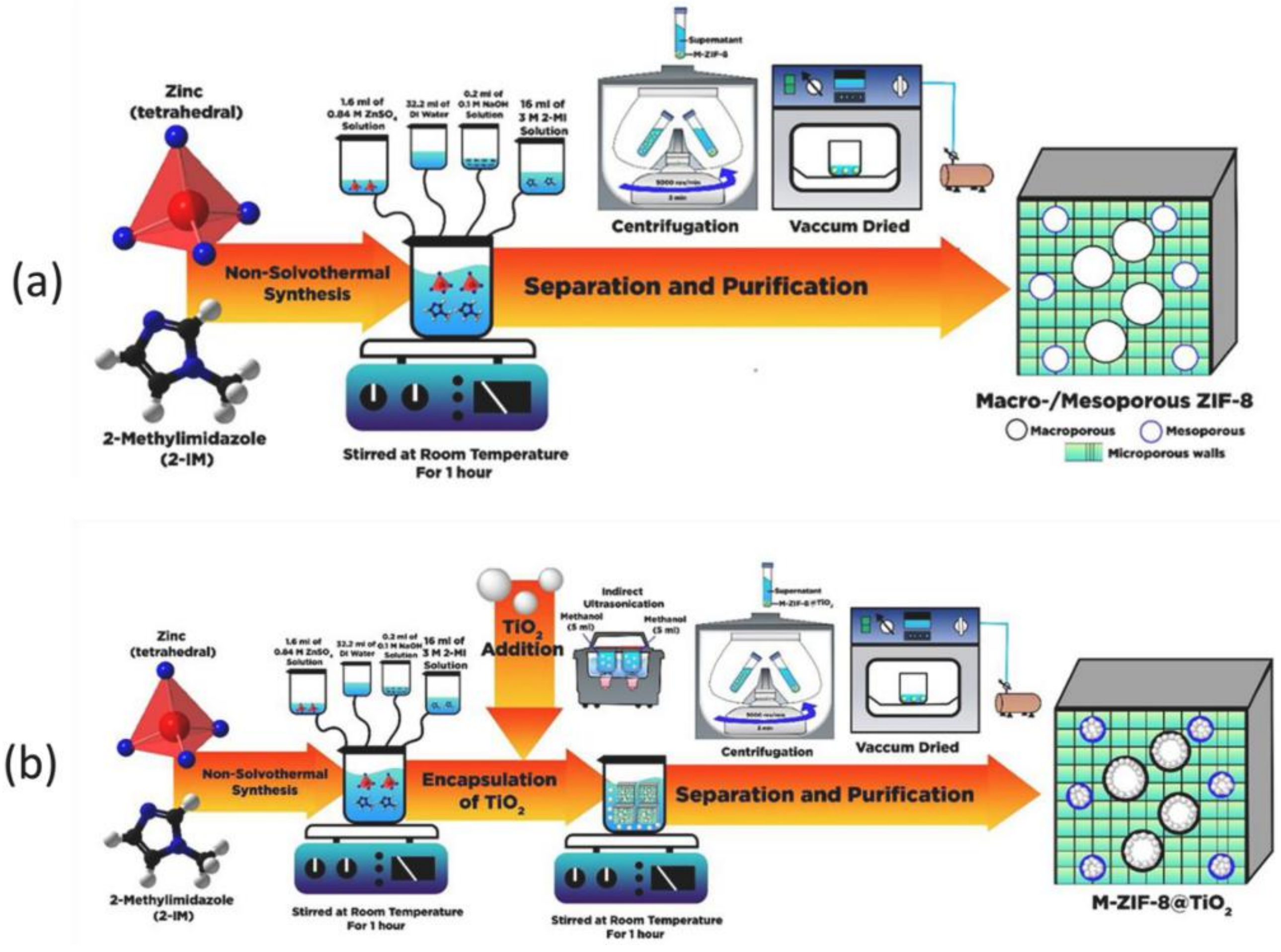

Fig. 2. Schematic procedure of (a) M−ZIF−8 and (b) M−ZIF−8@TiO_2 composites synthesis.

Electrochemical Workstation (Shanghai, China). The electrolyte was a solution containing 0.5 mol/L Na_2SO_4. A 0.5 mol/L Na_2SO_4 aqueous solution was used to make the electrolyte. Electrochemical impedance spectra (EIS) were performed at the open-circuit potential in 0.5 mol/L potassium ferricyanide/potassium ferrocyanide solution. The electrode was subjected to a 5 mV sinusoidal AC perturbation with a 0.5–100000 Hz frequency range.

2.4. Adsorption and photocatalytic degradation experiments

The present work studied the performance of adsorption/photocatalytic degradation of ZIF-8/ZIF-8@TiO2 and M−ZIF−8/M−ZIF−8@TiO2 to remove toxic organic dye CV from aqueous media. The adsorption experiment was conducted without UV light, while photocatalytic degradation was carried out in a UV lamp as the light source. The adsorption and photodegradation processes were conducted isothermally with an initial concentration of crystal violet 200 ppm. In the experiment, 1 g/L of M−ZIF−8/or M−ZIF−8@TiO_2/or ZIF-8/or ZIF-8@TiO_2 was dispersed CV solution. The flasks containing the mixture were placed in a thermal-controlled shaking water bath (Memmert WB-14) with/without UV irradiation during the experiments. Initially, the adsorption experiments were conducted in the dark condition. After the equilibrium point of adsorption had been reached, the photoirradiation process was conducted on the mixture using UV light at 360 nm. The experiments were conducted at room temperature (30 °C). The total adsorption and photodegradation time was 24 h. After the adsorption and photocatalytic degradation processes, the solids were separated from the mixture by centrifugation (Heraeus Labofuge 200) at 4900 rpm for 10 mins. The initial and equilibrium concentrations of CV were determined by UV-Visible Spectrophotometer (UV mini 1240 Shimadzu) at the maximum wavelength of CV (590 nm). The amount of CV adsorbed by ZIF-8 and ZIF-8@TiO2 at equilibrium condition was determined by equation (1) as follows:

$$qe = \frac{(Co - Ce)}{m} \times \mathrm{V} \tag{1}$$

Where q_e is the amount of CV adsorbed at equilibrium (mg/g), C_o is the concentration of CV in the liquid phase at initial condition (mg/L), C_e is the concentration of CV in the liquid phase at equilibrium condition (mg/L), V is the volume of CV solution (L), and m is the mass of adsorbent (g).

3. Characterization

The surface morphology and topography of M−ZIF−8 and M−ZIF−8@TiO_2 (5%) was evaluated through scanning electron microscopy (SEM). SEM images exhibit that M−ZIF−8 has a non-uniform structure with a truncated rhombic dodecahedron shape (Fig. 3). Fig. 3(b) manifests the SEM image of the M−ZIF−8@TiO2 composite, flower like morphology (Zhong et al., 2020) was obtained after incorporating TiO2 into ZIF-8 with no-obvious structural disintegration of ZIF-8. However, no-substantial TiO_2 was visible in the SEM Image, but the elemental composition of M−ZIF−8@TiO_2 (5%) composite by SEM-EDX indicates the presence of TiO_2. As shown in Table 1, five elements (C, N, Ti, O, and Zn) were discovered in the composite, which further specifies the success o TiO_2 integration towards MOFs. Moreover, the EDX mapping also detected five elements (C, N, Ti, O, and Zn), as seen in Fig. 3(c). The elemental distributions of C, O, Ti, Zn, and N are represented by green, red, yellow, blue, and purple. The presence of the elements Ti and O on the surface of the ZIF-8@TiO_2 composite in the mapping diagram suggests the successful distribution of TiO_2 nanospheres.

The phase purity and crystallinity M−ZIF−8, M−ZIF−8@TiO_2 (5%)

Table 1
Elemental Composition of M−ZIF−8 @TiO_2 based on SEM-EDX.

%Elemental Composition	M−ZIF−8	M−ZIF−8@TiO_2
C	49.73	48.29
N	30.23	27.27
Zn	12.94	11.8
O	7.1	9.38
Ti	–	3.25

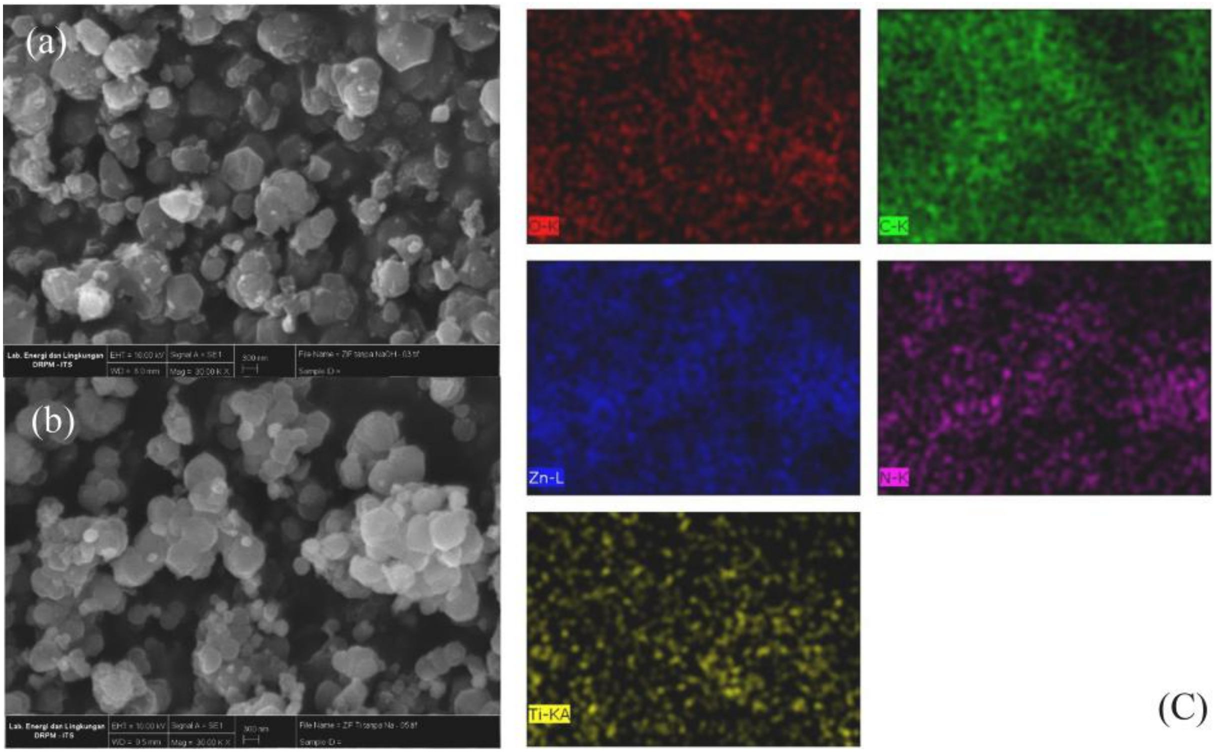

Fig. 3. Scanning Electron Microscopy (SEM) of M−ZIF−8 (a) and M−ZIF−8@TiO_2 (b); (c) SEM-EDX Mapping of M−ZIF−8@TiO_2.

and TiO_2 (anatase) were evaluated by X-ray diffraction (XRD) (Fig. 4 (a)). According to the XRD diffractograms, the synthesized M−ZIF−8 showed major characteristic reflections of the M−ZIF−8 sodalite structure at 2θ angles of 7.5°, 10.6°, 12.9°, 14.9°. 16.6°, and 18.2°, which attributed to the ZIF-8 planes including (220), (311), (422), (511), and (440) respectively and were consistent with the ZIF-8 single-crystal XRD pattern based on CCDC 602,542 (Tran et al., 2011). Meanwhile, the characteristic peak of TiO_2 was identified at 25.4°, 47.9°, 53.9°, 55.9°, and 62.7° which correspond to the (101), (200), (105), (211), and (204) crystal planes of TiO_2 (anatase) and matched with the TiO_2 simulated card (ICSD-50447) (Zhang et al., 2019). For the M−ZIF−8/TiO_2 (5%) composite, the XRD pattern simulated the major diffraction peaks of ZIF-8, with insufficient evidence of TiO_2 characteristic peaks owing to the weak intensity of the peak of TiO_2 (anatase) nanoparticles. Therefore, SEM and SEM-EDX were used to validate the XRD results further.

Fig. 4(b) shows the N_2 adsorption − desorption isotherms of the M−ZIF−8 and M−ZIF−8@TiO_2, respectively. The porous structure characteristic of M−ZIF−8 and M−ZIF−8@TiO_2 are listed in Tables 2 and 3. The N_2 sorption isotherm of M−ZIF−8 at 77 K exhibits Type I(a)/II isotherm (Lunardi et al., 2021). The swift N_2 uptake at a low relative pressure area ($P/P^o < 0.05$) indicates the MOF framework having a narrow microporous structure. Meanwhile, the subsequent step N_2 uptake at a high relative pressure ($P/Po > 0.95$) indicates the existence of large mesoporous and macroporous in MOF structures. The presence of large mesopores and macropores in the MOF structure can assist TiO_2 encapsulation in the MOF and facilitate the mass transport of CV to the internal structure of the M−ZIF−8@TiO_2. The M−ZIF−8 possesses a high BET surface area (2151 m2/g), while incorporating TiO_2 on the porous structure of M−ZIF−8 reduced the composite surface area to 854 m2/g. The decline in the composite porosity implies proper confinement of TiO_2 on M−ZIF−8.

Fig. 4(c). shows the FTIR spectra of M−ZIF−8 and M−ZIF−8@TiO_2. Vibration bands indicated the typical characteristic for ZIF-8 at 1427 cm^{-1}, 1419 $cm^{-1,}$ and 995 cm^{-1} that are assigned to C-N stretch, the bands at 1147 cm^{-1}, 1143 cm^{-1}, 1311 cm^{-1}, and 1308 cm^{-1} are attributed to imidazole bending, while the intense band at 420 cm^{-1} are associated with the Zn-N stretch (Hu et al., 2011). In addition, the typical vibration of the N-Ti-O bond was shown in 568 cm^{-1}, which demonstrates the successful growth of TiO_2 confined in ZIF-8 (Li et al., 2020; Zeng et al., 2016). The presence of the N-Ti-O bond indicates that the formation of ZIF-8@TiO_2 is not a simple physical mixing of the two chemical substances but a combination of chemical bonds.

The XPS survey spectrum of the M−ZIF−8@TiO_2 (5%) composite was shown in Fig. 5, indicating five elements, namely N, Ti, C, O, and Zn. In the C 1 s spectra, Fig. 5(a) indicates the appearance of C–C, and C–N coordination at 284.6 eV and 285.1 eV. Fig. 5(d) illustrates the O1s XPS spectrum of the composite. The major fittings peaks reveal the binding energy of Ti-O and Zn-OH at 529.8 and 531.4 eV, which also confirm TiO2 and ZIF-8 constructed the prepared composite. From Fig. 5(b), the XPS spectrum of Zn 2p from M−ZIF−8@TiO_2 (5%) revealed two peaks at 1021.3 eV and 1044.5 eV, which indicated the Zn $2p_{3/2}$ and Zn $2p_{1/2}$ binding energies (Cardoso et al., 2018). As present in Fig. 5(b), the Ti $2p_{3/2}$ and Ti $2p_{1/2}$ binding energies were displayed by two significant peaks at 458.4 eV and 464.1 eV, which implies oxidation states Ti^{4+} in M−ZIF−8@TiO_2 (5%) composite. Fig. 5(c) represents the N1s XPS spectrum. The peaks at 400.3 eV represent the binding energy of C–NH– and imidazole groups, while 399.6 eV peaks reveal N-Ti-O bonds in the composite. The N atoms in imidazole groups coordinated to replace the oxygen atoms in TiO_2, which verified the chemical bonding between TiO_2 and ZIF-8 nanoparticles (Pi et al., 2018). The presence of N-Ti-O coordination may illustrate the possibility of electron transfer from TiO2 to ZIF-8, catalyzing photogenerated charges and lowering the recombination rate compared to its counterpart. In order to justify the statement, photoluminescence (PL), transient photocurrent response and electrochemical impedance, and UV-diffuse reflectance spectra were employed for further validation.

UV-diffuse reflectance spectroscopy was utilized to determine the light absorption ability of the M−ZIF−8, TiO_2, and M−ZIF−8@TiO_2 (5%). As presented in Fig. 6, M−ZIF−8 has the optimum absorption wavelength at 228 nm, indicating M−ZIF−8 can only respond to the UV-light irradiation while TiO2 intensely responds to the visible irradiation since the measured optimum wavelength at 370 nm. When the integration of M−ZIF−8 and TiO_2 occurs, the composites reveal a broader absorption region that extends into the visible area owing to tight interaction between M−ZIF−8 and TiO_2, which ameliorate the composite light absorption capability and make the absorbed intensity in UV regions stronger.

The optical band gap of the-as-synthesized material can be measured using the Tauc Plot by modified the UV-DRS curve into $(\alpha h\nu)^2$ versus hν. The absorption coefficient, Planck constant, light frequency, proportionality constant, and bandgap are represented by h, v, A, and Eg. The band gaps of the samples would be determined by $(\alpha h\nu)^2$ versus hν (the absorbed light energy) (Zhong et al., 2020). The x-axis intercept of an extended tangential line from the linear portion of the curve was used to calculate the Eg value. Fig. 6(b) exhibit the estimated bandgap energies of M−ZIF−8, TiO_2 and M−ZIF−8@TiO_2 that are 5.14 eV, 3.33 eV and 2.98 eV respectively. The dramatical decrease of bandgap value indicates the applicability of the composites for light-harvesting in the visible range scope and ameliorates the photocatalytic system's efficiency.

Moreover, the measurement of the valence band and conduction band was also crucial to assessing the photocatalytic applicability. The linear extrapolation of the VB XPS spectrum leading edges to the baseline was utilized to evaluate the VB position of M−ZIF−8@TiO_2 (5%). As evaluated, ~2.1 eV was exhibited as the valence band of M−ZIF−8@TiO_2 (5%) while the CB position was measured on −0.87 eV, which is acquired from ($E_{VB} - E_g$). For CV and VB pristine TiO_2 and ZIF-

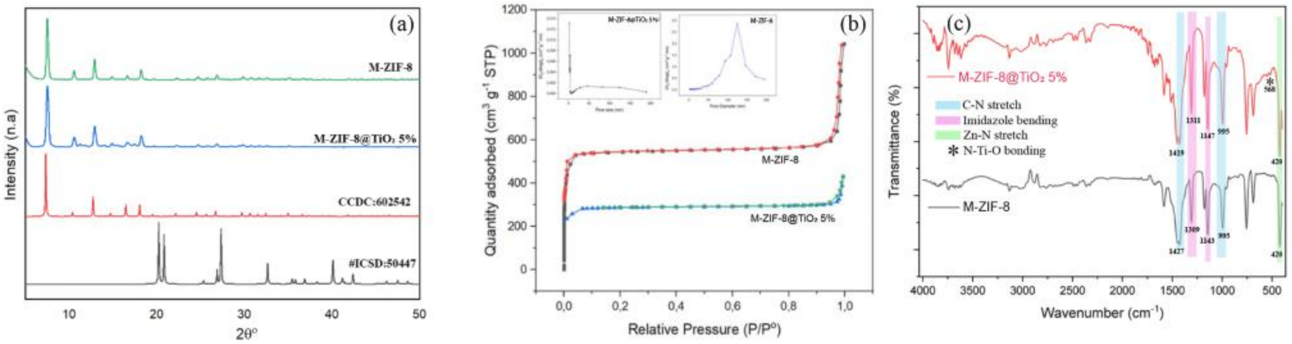

Fig. 4. Characterizations of the M−ZIF−8 and M−ZIF−8@TiO_2 5%. (a) Powder XRD patterns of the M−ZIF−8 and M−ZIF−8@TiO_2 as well as the simulated diffraction pattern from CCDC-602542 (ZIF-8) and ICSD-50447 (TiO_2-Anatase). (b) Nitrogen adsorption − desorption isotherms of M−ZIF−8 and M−ZIF−8@TiO_2 5%and at 77 K along with the Barrett-Joyner-Halenda (BJH) plot; (c) FTIR spectra of the M−ZIF−8 and M−ZIF−8@TiO_2.

Table 2
Comparison of Several Porous Structure of mesoporous/macroporous ZIF-8.

Sample	Synthesis Method of Mesoporous/Macroporous Structure	S_{BET} (m^2/g)	Pore Volume (cm^3/g)	Average pore Diameter (nm)	References
M−ZIF−8	NaOH Addition	2151	1.4998	124.66	This study
HpZIF-8	Structure Directing of PDDA (poly(diallyl dimethylammonium chloride)	242	–	-	(Chen et al., 2019)
Mesoporous ZIF-8	utilization of cetyltrimethylammonium bromide (CTAB) and amino-acid L-histidine as co-template	1134	1.30	-	(Jung et al., 2015)
HZIF-8	Polystyrene as directing template agent	1108	–	50–350	(Jing et al., 2018)
Mesoporous ZIF-8	Double solvent mediated overgrowth	1276	–	250	(Chou et al., 2015)

Table 3
Comparison of Several Porous Structure of ZIF-8@TiO_2.

Sample	S_{BET} (m^2/g)	Pore Volume (cm^3/g)	Average pore Diameter (nm)	References
M- ZIF-8@TiO_2 (anatase)	854	0.6023	25	This Study
ZIF-8@TiO_2	556.809	0.408	2.932	(Chen et al., 2019)
ZIF-8@TiO_2	668	0.81	1.2	(Zhang et al., 2019)
ZIF-8@TiO_2	253.882	–	-	(Chandra et al., 2016)

8, the following empirical formula was used (Zhang et al., 2019):

$$E_{VB} = X - - E_e + 0.5E_g \tag{2}$$

$$E_{CB} = E_{VB} - - E_g \tag{3}$$

Where variable "X" stands for the semiconductor's electronegativity, calculated based on the geometric mean of Mulliken electronegativity values of its constituent atoms. The arithmetic mean of the initial ionization energy and the first electron affinity represent the Mulliken electronegativity of an element (5.81 eV for TiO_2 and 2.36 eV for ZIF-8) (Zhang et al., 2019). E_e is the energy of free electrons on the hydrogen scale with a constant value of 4.5 eV vs. NHE (Wei et al., 2017), and E_g denotes the samples' bandgap energy measured by UV-DRS. Table 4. Represents E_g, E_{VB}, X and E_{CB} values of the composites and its counterpart.

In photocatalytic application, photoluminescence (PL) has been frequently utilized to evaluate charge carrier recombination rates between each sample. In the previous XPS characterization, it was reasonable to hypothesize the possible charge carrier migration path that establishes between TiO_2 and ZIF-8 (Zhang et al., 2019). Therefore, PL was applied to evaluate the charge carrier phenomenon. Fig. 6(d) shows the PL spectrum in which the PL intensity of TiO_2 is higher than the M−ZIF−8@TiO_2 (5%). The higher PL intensity indicates the greater possibility of the photogenerated carrier recombination in PL spectra. Pure TiO_2 provides a higher rate of electron-hole recombination. However, further incorporation of M−ZIF−8 has quenched the strong PL intensity, which indicates that the M−ZIF−8 addition effectively divides the electron-hole pairs by blocking the recombination of the photogenerated electron hole pairs, which implies the existence of a special path for carrier conveyance between TiO_2 and M−ZIF−8. Due to lower charge carriers' recombination rates, more electrons can be engaged in the photoreduction process.

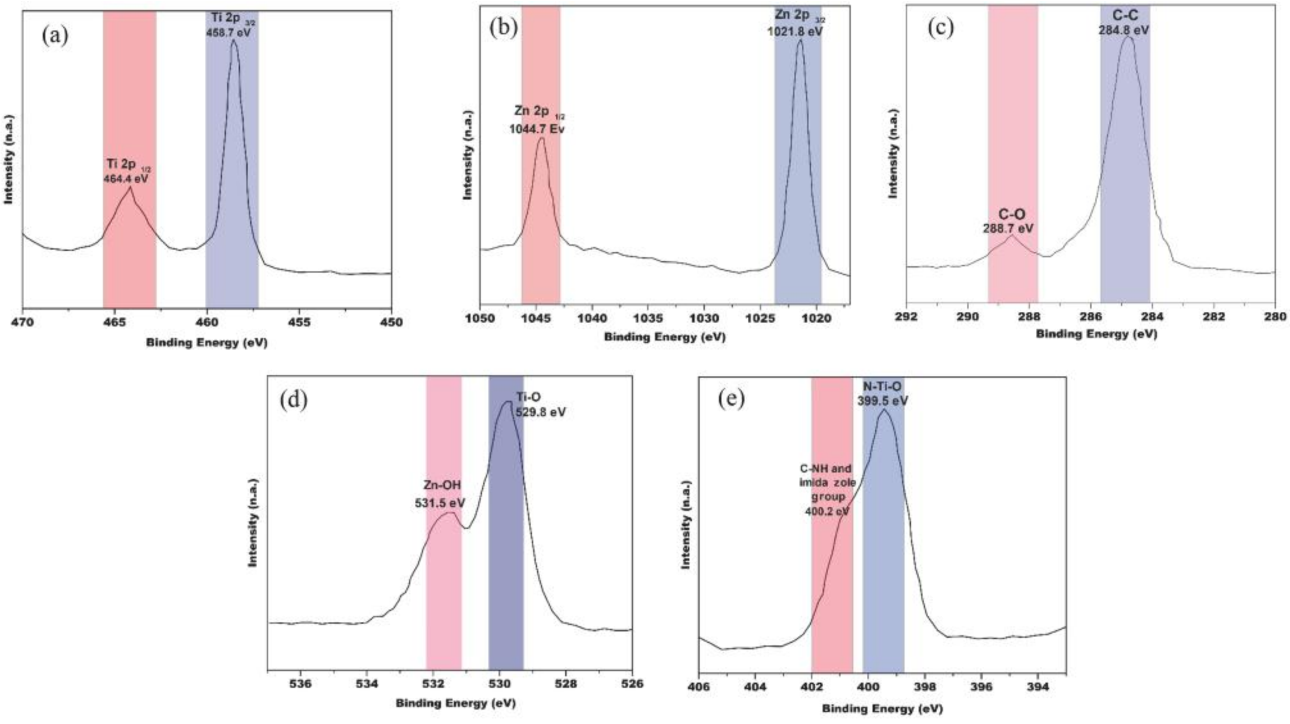

Fig. 5. The high-resolution XPS spectra for the Ti2p (a), Zn2p (b), C1s, (c), N1s (d), O1s (e) regions of M−ZIF−8@TiO_2 (5%).

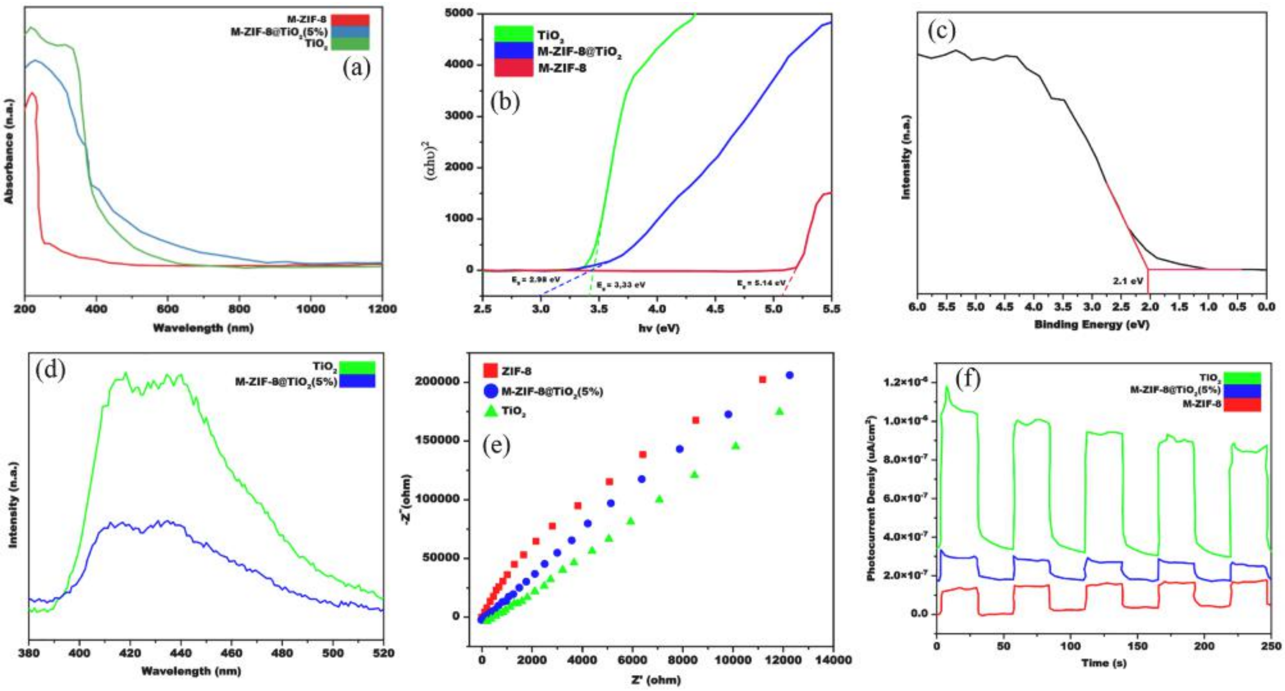

Fig. 6. (a). UV-Diffuse Reflectance Spectra of M−ZIF−8, M−ZIF−8@TiO_2 (5%) and TiO_2; (b). M−ZIF−8, M−ZIF−8@TiO_2 (5%) and TiO_2 optical band gap energy graphs; (c) the XPS Valence Band Spectrum For M−ZIF−8@TiO_2 (5%); (d) PL spectra; (e) Electrochemical impedance spectra and; (f) Photocurrent intensity of M−ZIF−8, TiO_2 and M−ZIF−8@TiO_2 (5%).

Table 4
Summary of electronegativity χ, band gap energy Eg (in eV), energy positions of band edges (EVBM and ECBM, in eV) of composite and its counterpart.

Materials	X (eV)[a]	Eg (eV)	E_{VB} (eV)[b]	E_{CB} (eV) [b]
ZIF-8	2.36	5.14	0.43	−4.71
TiO_2	5.81	3.33	2.98	−0.35
M−ZIF−8@TiO_2	n.d.	2.97	2.1	−0.87

Electrochemical Impedance Spectroscopy (EIS) and photocurrent studies of the as-synthesized samples were carried out to further comprehend composites' charge transfer property on the photocatalytic activities. Electrochemical impedance spectroscopy could visualize the photogenerated electron-hole pairs separation and interfacial charge transfer resistance (EIS). The EIS Nyquist plot would possess an arc shape when charged migration was present (Zhang et al., 2019). A smaller arc radius indicated higher charge transfer capabilities on the plot, which aided in separating photogenerated electron-hole pairs. Fig. 6(e) manifests the torque samples EIS spectrum. The arc radius of pristine TiO_2 and M−ZIF−8@TiO_2 (5%) are smaller than M−ZIF−8. This result revealed that composite fabrication could increase the electron transfer speed and efficiency of M−ZIF−8 and further ameliorate photocatalytic activity. Fig. 6(f) presents the photocurrent intensity of three materials. The M−ZIF−8 photocurrent response was the weakest of all. Although pristine TiO_2 had the maximum photocurrent density, their intensity faded over time after prolonged exposure to irradiation. The photocurrent intensity of the M−ZIF−8@TiO_2 (5%) composite is higher than that of M−ZIF−8, and it remains consistent over time, indicating that the composite is more stable than TiO_2. The reduction of electron-hole recombination achieved by incorporating TiO_2 onto ZIF-8 further increased photocatalytic efficacy.

4. Simultaneous adsorption and photocatalytic degradation of M−ZIF−8 and M−ZIF−8@TiO_2

4.1. Synthesis mechanism of NaOH on M−ZIF−8 and M−ZIF−8@TiO_2 formation

As analyzed, the morphological and porous structure clearly induced by the presence of NaOH during the synthesis of M−ZIF−8 and M−ZIF−8@TiO_2 (5%). Theoritically, the morphological structure of M−ZIF−8 is affected by several factors such as solvent, temperature, stoichiometric ligand/metal molar ratio, which can be attributed to the competition of ligand hydrolysis against the M−ZIF−8 formation (Jian et al., 2015). Hydrolysis in aqueous media and rapid synthesis of M−ZIF−8 limits the excess ligand to undergoes deprotonation and retard the nuclei construction. The role of NaOH as the basic compound is to increase the deprotonation rates of ligand. Since the excess ligand produced from reverse hydrolysis is different from the deprotonation rates of NaOH, resulting in an immature morphology of M−ZIF−8. Beneficially, this also can be the reason for the formation of mesoporous and microporous structures in M−ZIF−8, since the idea of mesoporous or macropores formation is the competition of ligand with other moieties or linker removal in structural framework to expand the size of pores.

The mechanism formation of M−ZIF−8 is divided into three steps: hydrolysis, coordination, and deprotonation (Fig. 7(a)). The first step of M−ZIF−8 formation through coordination of Zn^{2+} ions into deficient electron of pyridinic nitrogen of imidazole linker molecules which further induce the $Zn(Hmim)_n^{2+}$ ($1 \leq n \leq 4$) complex formation (Bustamante et al., 2014). Subsequently, the complexes begin to release the proton via deprotonation reaction with the assistance of basic species such as ammonia, excess linker, ion acetate (OAC^-), which in this case, the basic species was NaOH (Malekmohammadi et al., 2019). In the absence of these basic moieties, the deprotonation of ligand and the formation of M−ZIF−8 nucleus un-initiated in water since the pKa relatively high (~15–15.7). The solvent itself (in this case was water) acts as a mold to regulating the M−ZIFs structure via non-covalent

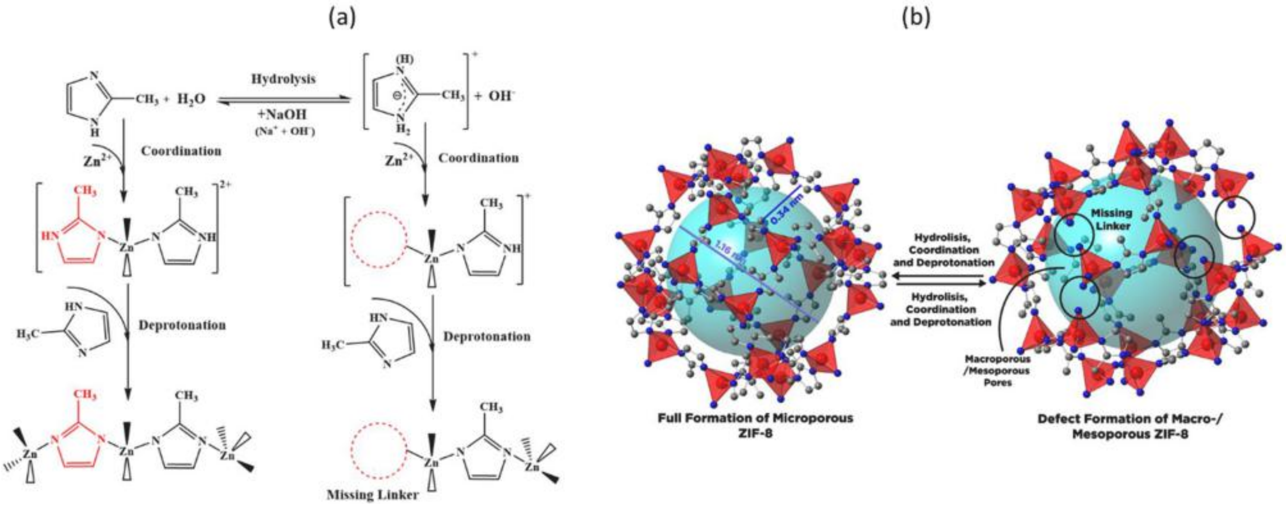

Fig. 7. (a) Mechanism formation of M−ZIF−8, and (b) defective formation on M−ZIF−8 structure.

coordination for bridging and pore stabilization throughout the cage's growth (Moh et al., 2011). Moh et al. (Moh et al., 2011) have investigated this phenomenon, and they found hydrogen linkage betwixt of the head of solvent consists of electronegative oxygen and the pyrrolic hydrogen of imidazole ring in linkers throughout the M−ZIF−8 formation.

Generally, the mechanism formation of M−ZIF−8 in the solution required the deprotonation of Hmim (mim$^-$ ions) to bridge the zinc ions to produce building units. However, the mechanism of M−ZIF−8 formation in water relatively complex because ligand strongly undergoes hydrolysis reaction in an aqueous solution. Initially, the production of $(H_2mim)^+$ begins with the reversible hydrolysis of the linker, and since the Hmim only present two structural isomers in water, including Hmim and $(H_2mim)^+$, the pH of the solution tend to increase. Then simultaneously, two phenomena occurred, namely complexation between zinc ions and linkers and reverse hydrolysis of linkers, which resulted in a drastic decrease in the pH of the solution because the hydrolysis reaction equilibrium shifted to the left side and the rapid use of Hmim during the coordination process. This is the purpose of increasing ligand to metal ratio to fulfill the requirement of deprotonation steps in aqueous solution to achieve higher M−ZIF−8 phase purity since the intermediate product of $Zn(Hmim)_n^{2+}$ ($1 \leq n \leq 4$) (pKa 10.3) has lower deprotonation compared to Hmim (Cravillon et al., 2011).

Eventually, the excess of Hmim can act as a deprotonation agent for protons cation removal to enable $Zn(Hmim)^{2+}$ complexation and generate M−ZIF−8 crystals. With the adjustment of time, the reaction may induce the morphology transformation of ZIF-8, which is caused by the different deprotonation steps, and the rate of excess Hmim and NaOH leads to the two types of M−ZIF−8 morphology formation. The truncated rhombic dodecahedron is likely generated from the deprotonation and rearrangement of complex coordination between zinc ions and excess ligand. With NaOH as a deprotonation agent and a high ligand to metal ratio, the rapid nucleation rate also increases, which might hinder the M−ZIF−8 growth significantly, causing the defective formation of ZIF-8 (Cravillon et al., 2011). Therefore, the defective formation and rearrangement of linkers in M−ZIF−8 induce macroporous/mesoporous structure (Fig. 7(b)). In comparison, this study provides a higher porous structure compared to those published ZIF-8/TiO_2 composites and mesoporous ZIF-8 (shown in Tables 2 and 3). Therefore, the addition of NaOH before the synthesis of M−ZIF−8 and M−ZIF−8@TiO_2 could increase the pore diameter and the surface area.

4.2. *Crystal violet isotherm and kinetic adsorption through M−ZIF−8 and ZIF-8*

In this study, Freundlich and Langmuir were employed to correlate the experimental adsorption data of CV onto M−ZIF−8 and ZIF-8. The mathematical expression of the Freundlich model is shown below (Al-Ghouti and Da'ana, 2020):

$$q_e = K_F \times Ce^{1/n} \tag{4}$$

where q_e is the amount of dyes adsorbed on the solid at equilibrium condition, Ce is the equilibrium concentration, and KF is Freundlich constants (mg/g (mg/L)-n), n is the heterogeneity of the system. The mathematical form of the well-known Langmuir isotherm is expressed as (Al-Ghouti and Da'ana, 2020):

$$q_e = \frac{q_{max}.K_L.C_e}{1 + K_L.C_e} \tag{5}$$

Parameters q_{max} and K_L are the Langmuir constants, representing the maximum adsorption capacity (mg/g) and the adsorption affinity (L/mg), respectively.

The experimental adsorption isotherm data of CV onto M−ZIF−8 and ZIF-8 based on Freundlich and Langmuir plots are given in Fig. 8(a). The Freundlich and Langmuir equation parameters obtained from the fitting of the experimental data are given in Table 5. From Fig. 8(a) and Table 5, it is proven that the Langmuir equation could represent the experimental data better than the Freundlich isotherm, indicated by a higher correlation coefficient (R^2). From Table 5 it can also be seen that the adsorption of CV with M−ZIF−8 has a higher q_e than with ZIF-8 without NaOH.

The pseudo-first-order and pseudo-second-order equations are utilized to represent the adsorption kinetic of CV onto M−ZIF−8 and ZIF-8. The differential form of the pseudo-first-order model is as follows:

$$\frac{dq_t}{dt} = k_1(q_e - q_t) \tag{6}$$

Integration of equation (6) resulting non-linear form of the pseudo-first-order as follows:

$$q_t = q_e(1 - \exp(-k_1 t)) \tag{7}$$

While the differential form of pseudo-second-order is written as follows

$$\frac{dq_t}{dt} = k_1(q_e - q_t)^2 \tag{8}$$

Integration of equation (8) produces the following equation

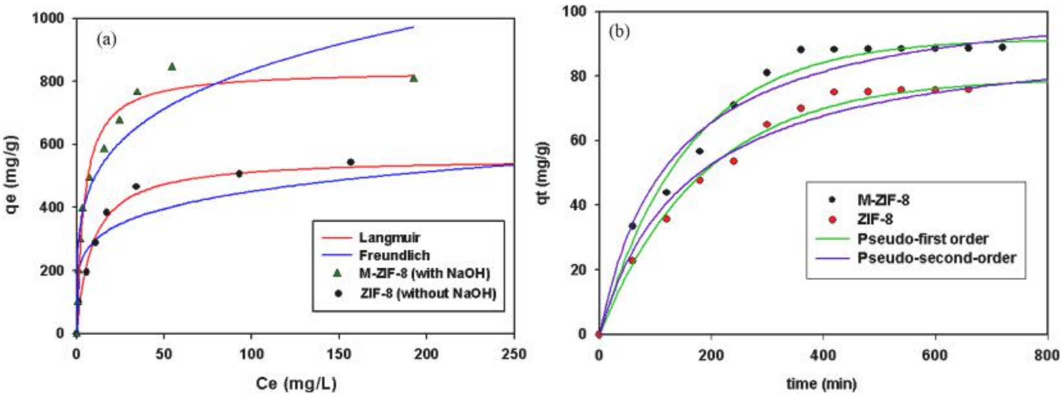

Fig. 8. (a) Isotherm and (b) Kinetic adsorption plot data of M−ZIF−8 and ZIF-8.

Table 5
Langmuir and Freundlich parameters for the CV adsorption onto M−ZIF−8 and ZIF-8.

Langmuir			Freundlich		
Parameters	M−ZIF−8	ZIF-8	Parameters	M−ZIF−8	ZIF-8
q_m (mg/g)	835.15	556.88	K_F (mg/g (mg/L)$^{-n}$)	290.61	191.40
K_L (L/mg)	0.2331	0.1139	n	4.3556	5.3690
R^2	0.9835	0.9868	R^2	0.8896	0.8868

$$q_t = q_e\left(\frac{q_e k_2 t}{1 + q_e k_2 t}\right) \tag{9}$$

Where q_t and q_e are the amounts of dye adsorbed by the solid at any time t and equilibrium condition, the parameters k_1 and k_2 can be assumed as the time constant for pseudo-first-order and pseudo-second-order, respectively. Fig. 8(b) shows that the system reached equilibrium in approximately 360 min. The parameters of Eqs. (6) and (7) obtained from the fitting of the experimental data are given in Table 6. According to the values of R^2, both equations could describe the kinetics adsorption of CV onto M−ZIF−8 and ZIF-8 equally well. The consistency of the parameter values is critical to determine the model's suitability to represent the adsorption kinetic data.

As mentioned before, the parameters k_1 and k_2 are time constant, indicating how fast the equilibrium condition of the adsorption system can be reached. Rapid equilibrium conditions can be indicated by high values of the parameters k_1 and k_2. The consistency of the values of parameters k_1 and k_2 with experiment kinetic data (Table 6) indicates the model's suitability to represent the adsorption kinetic of the system. As in the adsorption isotherm model, the parameter q_e represents the amount adsorbed at equilibrium condition. The parameter q_e obtained from the fitting of the experimental data should close to the value obtained from the experiment. Fig. 8(b) shows that the values of parameter q_e from the pseudo-first-order are close to the experimental data than the pseudo-second-order model (Table 6), indicating the validity of this model to represent the adsorption kinetic of CV onto M−ZIF−8 and ZIF-8.

4.3. *Effect of variables on dye photodegradation*

4.3.1. *Effect of pH on CV degradation*

The ability of the M−ZIF−8@TiO_2 composite to degrade organic compounds can be adjusted by varying the pH of the solution. The adsorption ability of the composite also influences the ability of the M−ZIF−8@TiO_2 to degrade organic compounds. In the case of degradation of some dyes such as CV, the effect of pH on the degradation efficiency is quite challenging to evaluate because the pH of the solution has multiple roles; pH affects the adsorption and degradation ability of the composite. By adjusting the solution pH, the deionization state of surface M−ZIF−8@TiO_2 can be varied, leading to the alteration of composite adsorption capacity. The availability of the hydroxyl radicals (OH*), which act as the oxidizing agent in the photodegradation process, is also strongly influenced by the solution pH. Hydroxyl radicals are available in excess amounts only at alkaline conditions, between the reaction of positive holes (h +) and hydroxyl ions (OH–), responsible for enhancing photocatalytic degradation rate. Hydroxyl ions are major species at neutral to high pH values, while positive holes are the major moieties at low pH.

Since pH plays a crucial role in evaluating the CV photodegradation efficiency, the photocatalytic behavior of ZIF-8@TiO_2 was evaluated over a broad pH range from 4 to 12 (Jing et al., 2014). At the same time, the color of the CV dye depends on the acidity or alkalinity of the solution. At a strongly acidic solution (<pH −1.0), the CV color is yellow, while above pH 10 the CV color turns blue. The inconsistent colors are the result of the different charged states of the CV molecules (Adams and Rosenstbin, 1914). Fig. 9(a) depicted that adsorption in higher alkaline solution gives better dye removal in M−ZIF−8. Fig. 9(b) shows the increased efficiency of CV adsorption/degradation with increased solution pH.

As mentioned earlier, the zero-point charge of M−ZIF−8@TiO_2 was found in pH 7.8, as seen in Fig. 9(c). Above the pH_{pzc}, the M−ZIF−8@TiO_2 surface was negatively charged owing to the adsorbed OH^-ions, while a positive charge was observed below the pH_{pzc}. Since crystal violet is a cationic dye, a strong interaction between negatively surface charged of M−ZIF−8@TiO_2 with the cationic CV became stronger, leading to an increase in the adsorption of CV on composite. At the same time, the presence of excess OH* at high pH accelerated the photocatalytic activity resulting in the reduction of CV due to

Table 6
Pseudo-first-order and second-order parameters for the adsorption of CV using ZIF-8.

Adsorbent	Pseudo first order			Pseudo second order		
	k_1 (min^{-1})	q_e (mg/g)	R^2	k_2 (g/mg min^{-1})	q_e (mg/g)	R^2
M−ZIF−8	0.0063	93.5229	0.9853	0.0001	107,1561	0.9627
M−ZIF−8@TiO_2 5%	0.0044	81.2559	0.9914	0.0001	94.7730	0.9677

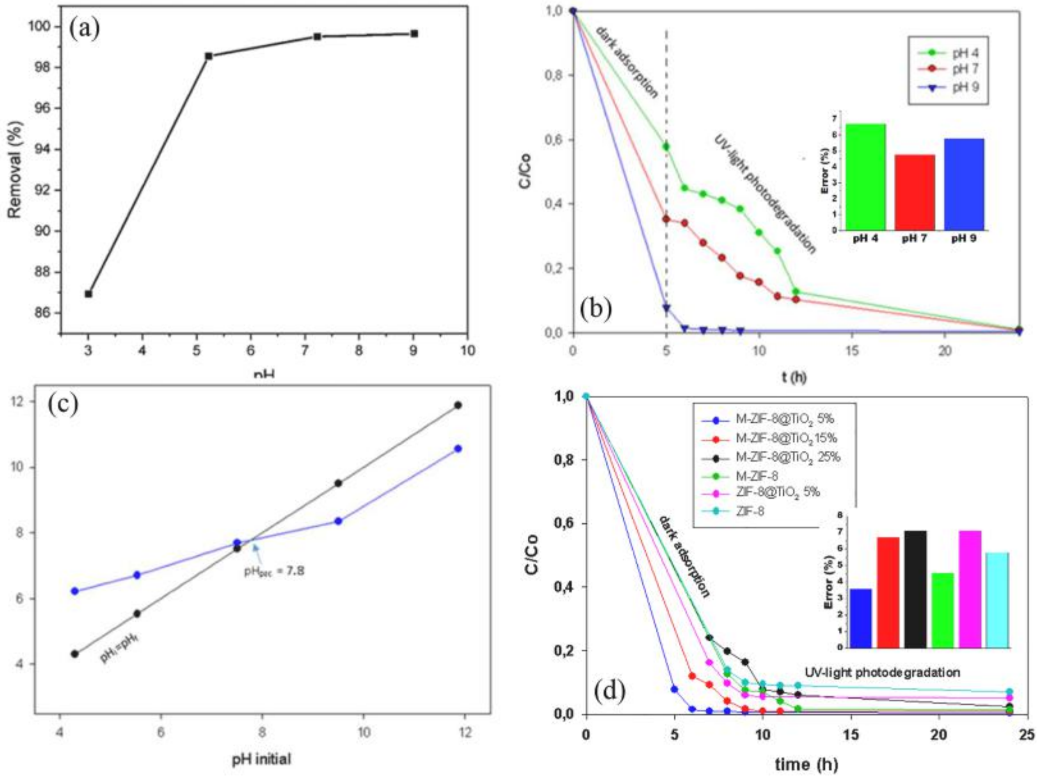

Fig. 9. Effect of various aspect on adsorption and photocatalytic dye degradation on M−ZIF−8; (a) Effect of pH on the adsorption of CV on M−ZIF−8; (b) Effect of pH on CV adsorption and photodegradation using M−ZIF−8@TiO_2 5%; (c) pHpzc of M−ZIF−8@TiO_2 5%; (d) Effect of mass ratio of TiO_2 incorporated to ZIF-8 and M_ZIF-8 on CV adsorption and photodegradation using M−ZIF−8@TiO2 5.

photocatalytic degradation.

4.3.2. *Effect of TiO_2 in M−ZIF−8*

The porosity of M−ZIF−8@TiO_2 would help refine mass transfer efficiency and ease the accessibility of active sites for photocatalytic degradation. This phenomenon was studied by varying the mass ratio of TiO_2 (5%,15%, 25%) incorporated into M−ZIF−8 (denoted as M−ZIF−8@TiO2 X%; X refers to the mass ratio of incorporated TiO_2). Appropriate composition of TiO_2 in M−ZIF−8@TiO_2 could improve the photoreactivity of the composite. The increase of photoreactivity due to increasing the specific surface area and promoting charge transfer (Du et al., 2021). Fig. 9(d) shows the influence of TiO_2 content in M−ZIF−8@TiO_2 on the degradation of CV. Fig. 9(d) clearly shows that M−ZIF−8@TiO_2 5% gave the best performance on the degradation of CV. The result indicates that excessive TiO_2 content results in catalysts aggregation, leading to fewer active sites for photodegradation, reducing light penetration, and leading to light scattering (Du et al., 2021).

4.3.3. *Effect of different coexisting Foreign Ions in Aquatic system*

In water, the CV solutions coexist with other ions. To explore the competitive effects of various coexisting ions, such as Cl^-, SO_4^{2-}, Na^+, K^+, Ca^{2+}, Al^{3+} on CV removal, the optimal conditions were used to conduct the photodegradation experiments. 10 ml of 200 mg/L CV solutions at pH ∼9 containing various amounts of NaCl, Na_2SO_4, KCl, $CaCl_2$, and $AlCl_3$ were prepared. Then, 10 mg of the M−ZIF−8/M−ZIF−8@TiO_2 was added into the Erlenmeyer with the prepared solution and shaken for 24 h (6 h in the dark and 18 h under UV light irradiation). After the removal reached equilibrium, the sample and the adsorbent were centrifuged for 10 min at 4900 rpm. Finally, the concentration of CV was tested by UV-Visible Spectrophotometer (UV mini 1240 Shimadzu) at 590 nm. The addition ions could compete for the adsorptive sites of M−ZIF−8 and M−ZIF 8@TiO_2 with CV. Notably, the negative impact of coexisting ions on CV adsorption and degradation followed the order: $Al^{3+} > Ca^{2+} > Na^+ > K^+ > SO_4^{2-}$ and Cl^- (Table 7). A drastic removal rate was observed with the addition of cations, especially aluminum. However, the anions, SO_4^{2-} and Cl^- showed almost no effect on the adsorption and degradation of CV due to the efficient synergistic effects of dye adsorption and photodegradation using M−ZIF−8/M−ZIF−8@TiO_2.

4.4. *Plausible mechanism of photocatalytic degradation of CV on M−ZIF−8@TiO_2*

Photo-induced hydroxyl radicals (OH*), superoxide anion radicals (O_2^{*-}), and holes (h^+) are all considered active species in the photocatalytic degradation. The free radical scavenging experiments were conducted to discover the major reactive species of M−ZIF−8@TiO_2 composite during the photodegradation of CV. 1.0 mM isopropanol (IPA), 1.0 mM benzoquinone (BQ), 1.0 mM ammonium oxalate (AO), and 1.0 mM of sodium azide (SA) were employed as scavengers for OH*,

Table 7
Effect of Different Coexisting Foreign Ions in Aquatic System.

Substance	Ion	Co (mmol/L)	Adsorbent	%Removal
NaCl	Cl^-	100	M−ZIF−8	97.12
			M−ZIF−8@TiO_2 5%	99.32
Na_2SO_4	SO_4^{2-}	100	M−ZIF−8	98.81
			M−ZIF−8@TiO_2 5%	99.48
NaCl	Na^+	15	M−ZIF−8	90.33
			M−ZIF−8@TiO_2 5%	91.86
KCl	K^+	15	M−ZIF−8	90.70
			M−ZIF−8@TiO_2 5%	90.93
$CaCl_2$	Ca^{2+}	15	M−ZIF−8	78.39
			M−ZIF−8@TiO_2 5%	84.13
$AlCl_3$	Al^{3+}	15	M−ZIF−8	32.53
			M−ZIF−8@TiO_2 5%	51.40

O_2^{*-}, h^+, and $^1O_{2,}$ respectively. As depicted in Fig. 10(a), CV degradation was evaluated dramatically and moderately obstructed by the presence of BQ and IPA, while insignificantly inhibited by the addition of AO and SA. The following sequence was determined based on the influence of the scavenger on the removal rate: BQ > IPA > AO > SA > No scavenger. In a nutshell, it is evidently proven that $O_2{*}^-$ is the crucial active species in the mechanism of CV.

Moreover, employing a 5.5-Dimethyl-1-1Pyrroline-N-Oxide (DMPO) quencher, ESR spectroscopic studies were performed to confirm the production of reactive oxygen species O_2^{*-} and OH*. No signal corresponding to the O2*- and OH* radicals were detected in the dark, as shown in Fig. 10(b). In the presence of UV irradiation, however, the signals for the four typical peaks of DMPO- O_2^{*-} (Jiang et al., 2015; Jin et al., 2021) and quartet pattern (1:2:2:1) of DMPO OH* were visible (Jin et al., 2021; Chou et al., 2021; Siao et al., 2019), and their intensity rose sharply with increased reaction time. This occurrence suggests that O_2^{*-} and OH* as the main active species has emerged.

Fig. 10(c) exhibits the plausible mechanism of M−ZIF−8@TiO₂ composite throughout the photodegradation system based on the result discussed previously. Regarding the UV-DRS spectrum, the electron excitation of TiO_2 and M−ZIF−8 during the UV-Irradiation (~360 nm) was limited due to a wide bandgap (3.33 and 5.14 eV, respectively). Meanwhile, the composite fabrication of M−ZIF−8@TiO_2 (5%) narrows the bandgap value (2.97 ev), facilitating the electron excitation and electron/hole pairs creation. The charge migration between MOF and semiconductors was observed, which remarkably limited the recombination of electron/hole. Through UV-light irradiation, the highest occupied molecular orbital (HOMO) of ZIF-8 initially transfers the electron towards the lowest unoccupied molecular orbital (LUMO) in ZIF-8. According to the previous characterization, the conduction band of TiO_2 is less negative than the HOMO potential in ZIF-8. Therefore, the conduction band of TiO_2 received the photogenerated electrons (e^-) from M−ZIF−8 conduction band while the valence band of TiO_2 transferred the holes to the M−ZIF−8 valence band. This phenomenon was significantly effective for photo-generated electron/hole pairs separation to boost photocatalytic activity. Eventually, the dissolved oxygen molecules, H_2O and OH^- substances, imprison the excited electron (e^-) and holes (h^+) in CB and VB, respectively. The plausible reaction mechanism was presented as follows (Liu et al., 2018; Dong et al., 2015; Chandra and Nath, 2017):

$$TiO_2 + hv \rightarrow TiO_2(e^- + \ h^+) \tag{10}$$

$$ZIF - 8 + hv \rightarrow ZI - 8(e^- + \ h^+) \tag{11}$$

$$TiO_2(e^-) + O_2 \rightarrow O_2^{*-} + TiO_2 \tag{12}$$

$$ZIF - 8(h^+) + H_2O/OH^- \rightarrow OH^* + ZIF - 8 \tag{13}$$

$$OH^*/O_2^{*-} + R - H \rightarrow R'^* + H_2O/O_2^{*-} \tag{14}$$

According to the trapping experiment result, O_2^{*-} are the major oxidant species in the CV degradation throughout the entire photocatalytic system. The superoxide anion (O_2^{-*}) and hydroxyl radicals (OH*) were generated after the transmission of photogenerated electrons toward oxygen molecules (O_2) and h^+ on the surface of TiO_2. Subsequently, the catalyst produced OH* and O2–* would benefit adsorbed CV mineralization through oxidation and decomposition on the photocatalyst surface. Meanwhile, the high specific surface and mesoporous structure of ZIF-8 particles also positively affect the photocatalytic degradation system of the composites. In common, there are three possible ways of ZIF-8 capture mechanism towards organic pollutants: (1). Open metal sites binding; (2). Electrostatic Interaction; (3). Functional groups interactions between organic pollutants and ZIF-8 (Kong et al., 2017). Therefore, it can be inferred that the integration of TiO_2 with the mesoporous structure of M−ZIF−8 provides excellent merits through a combination of the outstanding adsorption of MOF and photocatalytic advantageous from TiO_2 equipped with electron/hole recombine limitation.

4.5. M−ZIF−8 And M−ZIF−8@TiO₂ 5% reusability

The stability of the composite is also a vital factor in the commercial application of the material for contaminant degradation. The four-cycle experiment and XRD characterization was utilized to study the stability of the composites. The exhausted ZIF-8@TIO_2 was regenerated by three consecutive washing with water and ethanol and re-utilized for several photocatalytic degradations. Fig. 11 depicts the result of CV degradation over M−ZIF−8@TiO_2 (5%) throughout four cycles under UV-light irradiation. At present, the composite maintains its photocatalytic activity during four consecutive cycles.

Meanwhile, the XRD after the fourth cycle reveals no insignificant structure deterioration during the photocatalytic reaction based on the peak appearance, as seen in Fig. 11(c). However, it was considerably found intensity reduction at a few peaks of M−ZIF−8@$TiO_{2,}$ which indicates the adsorption slightly collapses the crystallinity of the composite. In this case, these findings exhibit catalytic activity, and the durability of the manufactured catalyst can be maintained throughout time. The slight reduction acquired during reaction might cause by the pore obstruction and weight during the washing process. Table 8. compares the photocatalytic performance of the as-synthesized catalyst in this work (M−ZIF−8@TiO_2 5%) with the several published TiO_2-based composite for dye elimination. The comparison is based on the adsorption and photodegradation ability. As presented, our study acquired a much greater capability of adsorption and photodegradation of CV than other published works. In which, this study disclosed the presence of mesoporous structure in ZIF-8 and the TiO_2 ability as

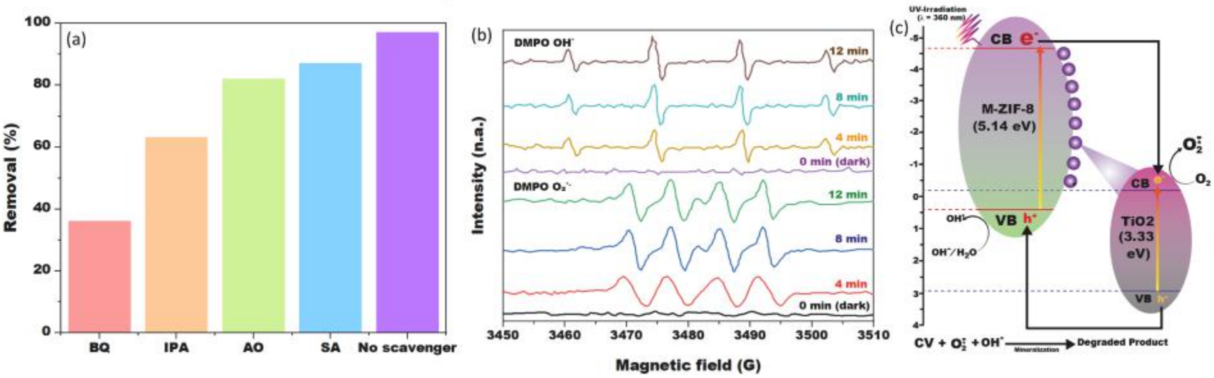

Fig. 10. (a). Effect of Quencher Reagent on the Photocatalytic Performance (b). DMPO spin-trapping EPR spectra for DMPO-O_2^- and DMPO-OH* (c). Mechanism of photocatalytic degradation of CV on M−ZIF−8@TiO_2.

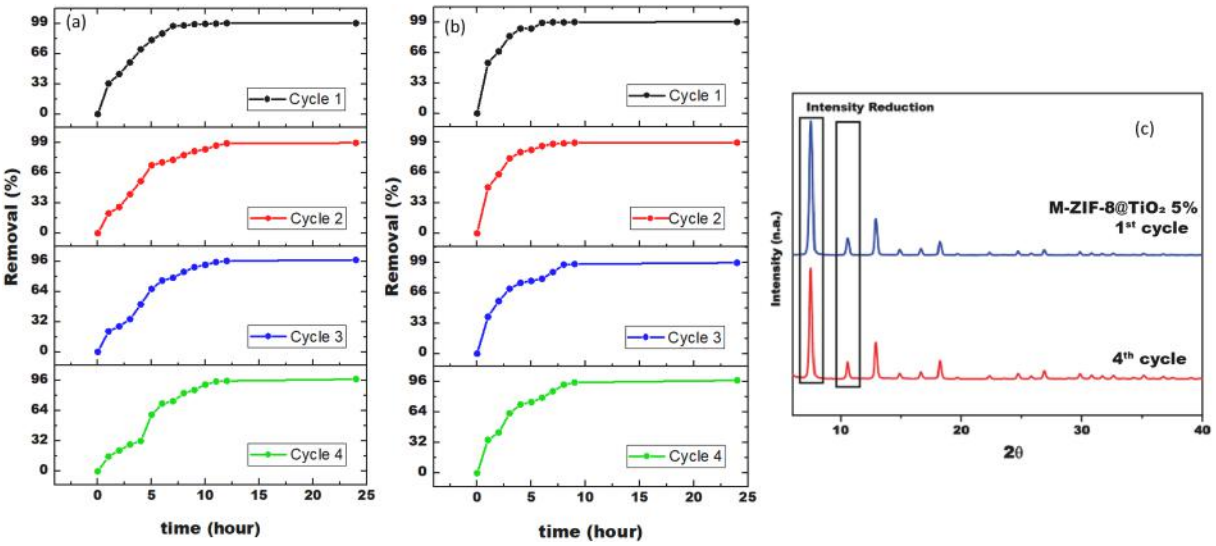

Fig. 11. (a) Cycle experiments of degradation of CV using M−ZIF−8 and (b) M−ZIF−8@TiO_2 5%; (c) XRD Performance of M−ZIF−8@TiO_2 5% After Several Cycle Experiments.

Table 8
Conspectus study of several composites based TiO_2 ability for CV photocatalytic adsorption and degradation.

Catalyst	CV Dosage (mg/L)	Reaction Parameter					Adsorption Conversion (%)	Degradation Conversion (%)	Ref.
		Catalyst Dosage (g/L)	pH	Dark Reaction Time (min)	Illumination Time (min)	Light Source			
MIL-101@TiO_2	20	5.5	n.d.	40	40	UV	51	48	(Chang et al., 2018)
F-TiO2(B)/fullerene	30	0.1	n.d.	30	120	vis	77.23		(Panahian et al., 2018)
Titanate Nanotube (TNT)	20	3	6.8	120	240	UV	80	15	(Mohanty et al., 2020)
T-WOAC	10	0.4	9	30	120	UV	31.77	67.24	(Gao et al., 2019)
TiO_2/CP SCA-3	10	0.2	6	30	120	UV	46	49	(Ullah et al., 2020)
10-Zr-TiO2-600	4,079.8	5	~7	1,440	1,320	UV	100%		(Vasic et al., 2016)
Graphene-TiO_2	100	0.05	6.5	15	20	UV	78		(Shende et al., 2018)
M−ZIF−8	200	1	9	360	1,080	UV	81.35	16.25	This study
M−ZIF−8@TiO_2 5%	200	1	9	300	1,140	UV	92.30	7.3	This study

photocatalytic catalyst act as perfect merits with higher removal activity.

5. Conclusion

A hierarchical porous of M−ZIF−8 has been successfully synthesized in an aqueous solution. By adding NaOH, macro-/mesoporous structures were acquired, still maintaining the mesoporous structure after the TiO_2 immobilization. The simultaneous adsorption and photocatalytic degradation were conducted in two different conditions. The adsorption experiments were conducted in the dark condition. After an equilibrium point was achieved, the suspension was photo-irradiated under UV light at 360 nm. M−ZIF−8@TiO_2 5% at pH 9 gave the best CV removal efficiency. After four consecutive experiments, M−ZIF−8@TiO_2 shows good performance and stability. The result of this study indicates that titanium dioxide embedded in ZIF-8 composite has excellent potential for removal of Crystal Violet from aqueous solution.

CRediT authorship contribution statement

Stefanny Angela: Investigation, Methodology, Visualization, Writing – original draft. **Valentino Bervia Lunardi:** Investigation, Methodology, Visualization, Writing – original draft. **Karissa Kusuma:** Investigation, Methodology. **Felycia Edi Soetaredjo:** Resources, Funding acquisition, Supervision. **Jindrayani Nyoo Putro:** Validation, Writing – review & editing. **Shella Permatasari Santoso:** Validation, Writing – review & editing. **Artik Elisa Angkawijaya:** Resources. **Jenni Lie:** Investigation, Formal analysis. **Chintya Gunarto:** Investigation, Formal analysis. **Alfin Kurniawan:** Formal analysis, Investigation. **Suryadi Ismadji:** Conceptualization, Resources, Funding acquisition, Supervision, Writing – review & editing.

Declaration of Competing Interest

The authors declare that they have no known competing financial interests or personal relationships that could have appeared to influence the work reported in this paper.

Acknowledgements

This study was supported by the Directorate of Research and Community Service, Deputy for Strengthening Research and Development, Ministry of Research and Technology/National Research and Innovation Agency, Number: 150E/WM01.5/N/2021.

References

Miklos, D.B., Remy, C., Jekel, M., Linden, K.G., Drewes, J.E., Hübner, U., 2018. Evaluation of advanced oxidation processes for water and wastewater treatment – A critical review. Water Res. 139, 118–131. https://doi.org/10.1016/j.watres.2018.03.042.

Kanakaraju, D., Glass, B.D., Oelgemöller, M., 2018. Advanced oxidation process-mediated removal of pharmaceuticals from water: A review. J. Environ. Manage. 219, 189–207. https://doi.org/10.1016/j.jenvman.2018.04.103.

Lu, S., Liu, L., Demissie, H., An, G., Wang, D., 2021. Design and application of metal-organic frameworks and derivatives as heterogeneous Fenton-like catalysts for organic wastewater treatment: A review. Environ. Int. 146, 106273. https://doi.org/10.1016/j.envint.2020.106273.

Vorontsov, A.V., 2019. Advancing Fenton and photo-Fenton water treatment through the catalyst design. J. Hazard. Mater. 372, 103–112. https://doi.org/10.1016/j.jhazmat.2018.04.033.

Yang, Y., Lu, X., Jiang, J., Ma, J., Liu, G., Cao, Y., Liu, W., Li, J., Pang, S., Kong, X., Luo, C., 2017. Degradation of sulfamethoxazole by UV, UV/H2O2 and UV/persulfate (PDS): Formation of oxidation products and effect of bicarbonate. Water Res. 118, 196–207. https://doi.org/10.1016/j.watres.2017.03.054.

Chen, D., Cheng, Y., Zhou, N., Chen, P., Wang, Y., Li, K., Huo, S., Cheng, P., Peng, P., Zhang, R., Wang, L.u., Liu, H., Liu, Y., Ruan, R., 2020. Photocatalytic degradation of organic pollutants using TiO2-based photocatalysts: A review. J. Clean. Prod. 268, 121725. https://doi.org/10.1016/j.jclepro.2020.121725.

Chen, Q., Yang, W., Zhu, J., Fu, L., Li, D., Zhou, L., 2020. Enhanced visible light photocatalytic activity of g-C3N4 decorated ZrO2-x nanotubes heterostructure for degradation of tetracycline hydrochloride. J. Hazard. Mater. 384, 121275. https://doi.org/10.1016/j.jhazmat.2019.121275.

Ong, C.B., Ng, L.Y., Mohammad, A.W., 2018. A review of ZnO nanoparticles as solar photocatalysts: Synthesis, mechanisms and applications. Renew. Sustain. Energy Rev. 81, 536–551. https://doi.org/10.1016/j.rser.2017.08.020.

Abdi, J., Yahyanezhad, M., Sakhaie, S., Vossoughi, M., Alemzadeh, I., 2019. Synthesis of porous TiO2/ZrO2 photocatalyst derived from zirconium metal organic framework for degradation of organic pollutants under visible light irradiation. J. Environ. Chem. Eng. 7 (3), 103096. https://doi.org/10.1016/j.jece:2019.103096.

Joseph, L., Jun, B.M., Jang, M., Park, C.M., Muñoz-Senmache, J.C., Hernández-Maldonado, A.J., Heyden, A., Yu, M., Yoon, Y., 2019. Removal of contaminants of emerging concern by metal-organic framework nanoadsorbents: A review. Chem. Eng. J. 369, 928–946. https://doi.org/10.1016/j.cej.2019.03.173.

Furukawa, H., Cordova, K.E., O'Keeffe, M., Yaghi, O.M., 2013. The chemistry and applications of metal-organic frameworks. Science 80, 341. https://doi.org/10.1126/science.1230444.

Guan, H.Y., LeBlanc, R.J., Xie, S.Y., Yue, Y., 2018. Recent progress in the syntheses of mesoporous metal–organic framework materials. Coord. Chem. Rev. 369, 76–90. https://doi.org/10.1016/j.ccr.2018.05.001.

Zhang, W., Liu, Y., Lu, G., Wang, Y., Li, S., Cui, C., Wu, J., Xu, Z., Tian, D., Huang, W., DuCheneu, J.S., Wei, W.D., Chen, H., Yang, Y., Huo, F., 2015. Mesoporous metal-organic frameworks with size-, shape-, and space-distribution-controlled pore structure. Adv. Mater. 27 (18), 2923–2929. https://doi.org/10.1002/adma.v27.1810.1002/adma.201405752.

Jing, P., Zhang, S.-Y., Chen, W., Wang, L., Shi, W., Cheng, P., 2018. A Macroporous Metal-Organic Framework with Enhanced Hydrophobicity for Efficient Oil Adsorption. Chem. – A Eur. J. 24 (15), 3754–3759. https://doi.org/10.1002/chem.201704929.

Wu, Y.-N., Zhou, M., Zhang, B., Wu, B., Li, J., Qiao, J., Guan, X., Li, F., 2014. Amino acid assisted templating synthesis of hierarchical zeolitic imidazolate framework-8 for efficient arsenate removal. Nanoscale. 6 (2), 1105–1112. https://doi.org/10.1039/C3NR04390H.

Jung, B.K., Jun, J.W., Hasan, Z., Jhung, S.H., 2015. Adsorptive removal of p-arsanilic acid from water using mesoporous zeolitic imidazolate framework-8. Chem. Eng. J. 267, 9–15. https://doi.org/10.1016/j.cej.2014.12.093.

Chou, L.-Y., Hu, P., Zhuang, J., Morabito, J.V., Ng, K.C., Kao, Y.-C., Wang, S.-C., Shieh, F.-K., Kuo, C.-H., Tsung, C.-K., 2015. Formation of hollow and mesoporous structures in single-crystalline microcrystals of metal-organic frameworks via double-solvent mediated overgrowth. Nanoscale. 7 (46), 19408–19412. https://doi.org/10.1039/C5NR06532A.

Chen, X., Jiang, X., Yin, C., Zhang, B., Zhang, Q., 2019. Facile fabrication of hierarchical porous ZIF-8 for enhanced adsorption of antibiotics. J. Hazard. Mater. 367, 194–204. https://doi.org/10.1016/j.jhazmat.2018.12.080.

Wang, M., Ioccozia, J., Sun, L., Lin, C., Lin, Z., 2014. Inorganic-modified semiconductor TiO2 nanotube arrays for photocatalysis. Energy Environ. Sci. 7 (7), 2182–2202. https://doi.org/10.1039/C4EE00147H.

Xu, Y.-F., Wang, X.-D., Liao, J.-F., Chen, B.-X., Chen, H.-Y., Kuang, D.-B., 2018. Bin Kuang, Amorphous-TiO2-Encapsulated CsPbBr 3 Nanocrystal Composite Photocatalyst with Enhanced Charge Separation and CO2 Fixation. Adv. Mater. Interfaces. 5 (22), 1801015. https://doi.org/10.1002/admi.v5.2210.1002/admi.201801015.

Chandra, R., Mukhopadhyay, S., Nath, M., 2016. TiO2@ZIF-8: A novel approach of modifying micro-environment for enhanced photocatalytic dye degradation and high usability of TiO2 nanoparticles. Mater. Lett. 164, 571–574. https://doi.org/10.1016/j.matlet.2015.11.018.

Liu, J., Chen, L., Cui, H., Zhang, J., Zhang, L.i., Su, C.-Y., 2014. Applications of metal-organic frameworks in heterogeneous supramolecular catalysis. Chem. Soc. Rev. 43 (16), 6011–6061. https://doi.org/10.1039/C4CS00094C.

Akbari Beni, F., Gholami, A., Ayati, A., Niknam Shahrak, M., Sillanpää, M., 2020. UV-switchable phosphotungstic acid sandwiched between ZIF-8 and Au nanoparticles to improve simultaneous adsorption and UV light photocatalysis toward tetracycline degradation. Microporous Mesoporous Mater. 303, 110275. https://doi.org/10.1016/j.micromeso.2020.110275.

X. Yang, Z. Wen, Z. Wu, X.L.-I.C. Frontiers, undefined 2018, Synthesis of ZnO/ZIF-8 hybrid photocatalysts derived from ZIF-8 with enhanced photocatalytic activity, Pubs.Rsc.Org. (n.d.). https://pubs.rsc.org/no/content/articlehtml/2018/qi/c7qi00752c (accessed June 27, 2021).

Fan, G., Luo, J., Guo, L., Lin, R., Zheng, X., Snyder, S.A., 2018. Doping Ag/AgCl in zeolitic imidazolate framework-8 (ZIF-8) to enhance the performance of photodegradation of methylene blue. Chemosphere. 209, 44–52. https://doi.org/10.1016/j.chemosphere.2018.06.036.

Liu, A., Yu, C., Lin, J., Sun, G., Xu, G., Huang, Y., Liu, Z., Tang, C., 2019. Construction of CuInS2@ZIF-8 nanocomposites with enhanced photocatalytic activity and durability. Mater. Res. Bull. 112, 147–153. https://doi.org/10.1016/j.materresbull.2018.12.020.

Zhong, W.-L., Li, C., Liu, X.-M., Bai, X.-K., Zhang, G.-S., Lei, C.-X., 2020. Liquid phase deposition of flower-like TiO2 microspheres decorated by ZIF-8 nanoparticles with enhanced photocatalytic activity. Microporous Mesoporous Mater. 306, 110401 https://doi.org/10.1016/j.micromeso.2020.110401.

U.P.N. Tran, K.K.A. Le, N.T.S. Phan, ACS Catal., 2011, 1, 120 CrossRef CAS;(b) K. Park, Z. Ni, AP Cote, J.-T. Choi, J. Uribe-Romo, HK Chae, R. Huang, MO Keeffe and OM Yaghi, Proc. Natl. Acad. Sci. USA. 103 (2006) 10186.

Zhang, M., Shang, Q., Wan, Y., Cheng, Q., Liao, G., Pan, Z., 2019. Self-template synthesis of double-shell TiO2@ZIF-8 hollow nanospheres via sonocrystallization with enhanced photocatalytic activities in hydrogen generation. Appl. Catal. B Environ. 241, 149–158. https://doi.org/10.1016/j.apcatb.2018.09.036.

Lunardi, V.B., Gunawan, F., Soetaredjo, F.E., Santoso, S.P., Chen, C.H., Yuliana, M., Kurniawan, A., Lie, J., Angkawijaya, A.E., Ismadji, S., 2021. Efficient One-Step Conversion of a Low-Grade Vegetable Oil to Biodiesel over a Zinc Carboxylate Metal-Organic Framework. ACS Omega. 6, 1834–1845. https://doi.org/10.1021/acsomega.0c03826.

Hu, Y., Kazemian, H., Rohani, S., Huang, Y., Song, Y., 2011. In situ high pressure study of ZIF-8 by FTIR spectroscopy. Chem. Commun. 47, 12694–12696. https://doi.org/10.1039/c1cc15525c.

Li, R., Li, W., Jin, C., He, Q., Wang, Y., 2020. Fabrication of ZIF-8@TiO2 micron composite via hydrothermal method with enhanced absorption and photocatalytic activities in tetracycline degradation. J. Alloys Compd. 825, 154008 https://doi.org/10.1016/j.jallcom.2020.154008.

Zeng, X., Huang, L., Wang, C., Wang, J., Li, J., Luo, X., 2016. Sonocrystallization of ZIF-8 on Electrostatic Spinning TiO2 Nanofibers Surface with Enhanced Photocatalysis Property through Synergistic Effect. ACS Appl. Mater. Interfaces. 8, 20274–20282. https://doi.org/10.1021/acsami.6b05746.

Cardoso, J.C., Stulp, S., de Brito, J.F., Flor, J.B.S., Frem, R.C.G., Zanoni, M.V.B., 2018. MOFs based on ZIF-8 deposited on TiO2 nanotubes increase the surface adsorption of CO2 and its photoelectrocatalytic reduction to alcohols in aqueous media. Appl. Catal. B Environ. 225, 563–573. https://doi.org/10.1016/j.apcatb.2017.12.013.

Pi, H., Zhang, D., Zhang, X., Jin, Z., Zhang, L., Cui, X., Zheng, W., 2018. Passivation of the surface imperfection of TiO2 by using ZIF-8 for efficient carrier separation/transfer. Dalt. Trans. 47, 209–214. https://doi.org/10.1039/C7DT03972G.

Wei, Y., Cheng, G., Xiong, J., Xu, F., Chen, R., 2017. Positive Ni(HCO3)2 as a Novel Cocatalyst for Boosting the Photocatalytic Hydrogen Evolution Capability of Mesoporous TiO2 Nanocrystals. ACS Sustain. Chem. Eng. 5, 5027–5038. https://doi.org/10.1021/acssuschemeng.7b00417.

Jian, M., Liu, B., Liu, R., Qu, J., Wang, H., Zhang, X., 2015. Water-based synthesis of zeolitic imidazolate framework-8 with high morphology level at room temperature. RSC Adv. 5, 48433–48441. https://doi.org/10.1039/c5ra04033g.

Bustamante, E.L., Fernández, J.L., Zamaro, J.M., 2014. Influence of the solvent in the synthesis of zeolitic imidazolate framework-8 (ZIF-8) nanocrystals at room temperature. J. Colloid Interface Sci. 424, 37–43. https://doi.org/10.1016/j.jcis.2014.03.014.

Malekmohammadi, M., Fatemi, S., Razavian, M., Nouralishahi, A., 2019. A comparative study on ZIF-8 synthesis in aqueous and methanolic solutions: Effect of temperature and ligand content. Solid State Sci. 91, 108–112. https://doi.org/10.1016/j.solidstatesciences.2019.03.022.

Moh, P.Y., Cubillas, P., Anderson, M.W., Attfield, M.P., 2011. Revelation of the molecular assembly of the nanoporous metal organic framework ZIF-8. J. Am. Chem. Soc. 133, 13304–13307. https://doi.org/10.1021/ja205900f.

Cravillon, J., Nayuk, R., Springer, S., Feldhoff, A., Huber, K., Wiebcke, M., 2011. Controlling zeolitic imidazolate framework nano- and microcrystal formation: Insight into crystal growth by time-resolved in situ static light scattering. Chem. Mater. 23, 2130–2141. https://doi.org/10.1021/cm103571y.

Cravillon, J., Schröder, C.A., Nayuk, R., Gummel, J., Huber, K., Wiebcke, M., 2011. Fast nucleation and growth of ZIF-8 nanocrystals monitored by time-resolved in situ small-angle and wide-angle X-ray scattering. Angew. Chemie – Int. Ed. 50, 8067–8071. https://doi.org/10.1002/anie.201102071.

Al-Ghouti, M.A., Da'ana, D.A., 2020. Guidelines for the use and interpretation of adsorption isotherm models: A review. J. Hazard. Mater. 393, 122383 https://doi.org/10.1016/j.jhazmat.2020.122383.

Jing, H.P., Wang, C.C., Zhang, Y.W., Wang, P., Li, R., 2014. Photocatalytic degradation of methylene blue in ZIF-8. RSC Adv. 4, 54454–54462. https://doi.org/10.1039/c4ra08820d.

Adams, E.Q., Rosenstbin, L., 1914. The color and ionization of crystal-violet. J. Am. Chem. Soc. 36, 1452–1473. https://doi.org/10.1021/ja02184a014.

Du, C., Zhang, Z., Yu, G., Wu, H., Chen, H., Zhou, L., Zhang, Y., Su, Y., Tan, S., Yang, L., Song, J., Wang, S., 2021. A review of metal organic framework (MOFs)-based materials for antibiotics removal via adsorption and photocatalysis. Chemosphere. 272, 129501 https://doi.org/10.1016/j.chemosphere.2020.129501.

Jiang, Y.-R., Lin, H.-P., Chung, W.-H., Dai, Y.-M., Lin, W.-Y., Chen, C.-C., 2015. Controlled hydrothermal synthesis of BiOxCly/BiOmIn composites exhibiting visible-light photocatalytic degradation of crystal violet. J. Hazard. Mater. 283, 787–805. https://doi.org/10.1016/j.jhazmat.2014.10.025.

Jin, J.-C., Yang, M., Zhang, Y.-L., Dutta, A., Xie, C.-G., Kumar, A., 2021. Integration of mixed ligand into a multivariate metal-organic framework for enhanced UV-light photocatalytic degradation of Rhodamine B. J. Taiwan Inst. Chem Eng.

Chou, Y.-C., Lin, Y.-Y., Lu, C.-S., Liu, F.-Y., Lin, J.-H., Chen, F.-H., Chen, C.-C., Wu, W.-T., 2021. Controlled hydrothermal synthesis of BiOxCly/BiOmBrn/g-C3N4 composites exhibiting visible-light photocatalytic activity. J. Environ. Manage. 297, 113256 https://doi.org/10.1016/j.jenvman.2021.113256.

Siao, C.-W., Lee, W.-L.-W., Dai, Y.-M., Chung, W.-H., Hung, J.-T., Huang, P.-H., Lin, W.-Y., Chen, C.-C., 2019. BiOxCly/BiOmBrn/BiOpIq/GO quaternary composites: syntheses and application of visible-light-driven photocatalytic activities. J. Colloid Interface Sci. 544, 25–36.

Liu, X., Zhang, J., Dong, Y., Li, H., Xia, Y., Wang, H., 2018. A facile approach for the synthesis of Z-scheme photocatalyst ZIF-8/g-C3N4 with highly enhanced photocatalytic activity under simulated sunlight. New J. Chem. 42, 12180–12187. https://doi.org/10.1039/C8NJ01782D.

Dong, S., Feng, J., Fan, M., Pi, Y., Hu, L., Han, X., Liu, M., Sun, J., Sun, J., 2015. Recent developments in heterogeneous photocatalytic water treatment using visible light-responsive photocatalysts: a review. Rsc Adv. 5, 14610–14630.

Chandra, R., Nath, M., 2017. Multi-Core–shell TiO2NPs@ZIF-8 Composite for Enhanced Photocatalytic Degradation and Adsorption of Methylene Blue and Rhodamine-B. ChemistrySelect. 2, 7711–7722. https://doi.org/10.1002/slct.201701195.

Kong, R.-M., Zhao, Y., Zheng, Y., Qu, F., 2017. Facile synthesis of ZnO/CdS@ ZIF-8 core–shell nanocomposites and their applications in photocatalytic degradation of organic dyes. RSC Adv. 7, 31365–31371.

Chang, N., Zhang, H., Shi, M.S., Li, J., Yin, C.J., Wang, H.T., Wang, L., 2018. Regulation of the adsorption affinity of metal-organic framework MIL-101 via a TiO2 coating strategy for high capacity adsorption and efficient photocatalysis. Microporous Mesoporous Mater. 266, 47–55. https://doi.org/10.1016/J.MICROMESO.2018.02.051.

Panahian, Y., Arsalani, N., Nasiri, R., 2018. Enhanced photo and sono-photo degradation of crystal violet dye in aqueous solution by 3D flower like F-TiO2(B)/fullerene under visible light. J. Photochem. Photobiol. A Chem. 365, 45–51. https://doi.org/10.1016/J.JPHOTOCHEM.2018.07.035.

Mohanty, S., Moulick, S., Maji, S.K., 2020. Adsorption/photodegradation of crystal violet (basic dye) from aqueous solution by hydrothermally synthesized titanate nanotube (TNT). J. Water Process Eng. 37, 101428 https://doi.org/10.1016/J.JWPE.2020.101428.

Gao, Z., Wu, Z., Chen, X., Yang, X., 2019. Effective synthesis of nanoscale anatase TiO2 single crystals using activated carbon template to enhance the photodegradation of crystal violet. Appl. Organomet. Chem. 33, e4664 https://doi.org/10.1002/AOC.4664.

Ullah, R., Sun, J., Gul, A., Bai, S., 2020. One-step hydrothermal synthesis of TiO2-supported clinoptilolite: An integrated photocatalytic adsorbent for removal of crystal violet dye from aqueous media. J. Environ. Chem. Eng. 8, 103852 https://doi.org/10.1016/J.JECE.2020.103852.

Vasic, M.B., Ranđelović, M.S., Momčilović, M.Z., Matović, B., Zarubica, A.R., 2016. Degradation of crystal violet over heterogeneous TiO2-based catalysts: The effect of process parameters. Process. Appl. Ceram. 10, 189–198. https://doi.org/10.2298/PAC1603189V.

Shende, T.P., Bhanvase, B.A., Rathod, A.P., Pinjari, D.V., Sonawane, S.H., 2018. Sonochemical synthesis of Graphene-Ce-TiO2 and Graphene-Fe-TiO2 ternary hybrid photocatalyst nanocomposite and its application in degradation of crystal violet dye. Ultrason. Sonochem. 41, 582–589. https://doi.org/10.1016/J.ULTSONCH.2017.10.024.